A&A 587, A45 (2016)
DOI: 10.1051/0004-6361/201527644

Astronomy & Astrophysics

The spatially resolved correlation between [NII] 205 μm line emission and the 24 μm continuum in nearby galaxies

T. M. Hughes[1,2], M. Baes[2], M. R. P. Schirm[3], T. J. Parkin[3], R. Wu[4], I. De Looze[2], C. D. Wilson[3], S. Viaene[2], G. J. Bendo[5], A. Boselli[6], D. Cormier[7], E. Ibar[1], O. Ł. Karczewski[8], N. Lu[9], and L. Spinoglio[10]

[1] Instituto de Física y Astronomía, Universidad de Valparaíso, Avda. Gran Bretaña 1111, Valparaíso, Chile
e-mail: thomas.hughes@uv.cl
[2] Sterrenkundig Observatorium, Universiteit Gent, Krijgslaan 281-S9, 9000 Gent, Belgium
[3] Department of Physics & Astronomy, McMaster University, Hamilton, Ontario L8S 4M1, Canada
[4] Department of Astronomy, the University of Tokyo, Bunkyo-ku, 113-0033 Tokyo, Japan
[5] UK ALMA Regional Centre Node, Jodrell Bank Centre for Astrophysics, School of Physics and Astronomy, University of Manchester, Oxford Road, Manchester M13 9PL, UK
[6] Laboratoire d'Astrophysique de Marseille, Université d'Aix-Marseille and CNRS, UMR7326, 13388 Marseille Cedex 13, France
[7] Institut für theoretische Astrophysik, Zentrum für Astronomie der Universität Heidelberg, Albert-Ueberle 2, 69120 Heidelberg, Germany
[8] Department of Physics & Astronomy, University of Sussex, Brighton, BN1 9QH, UK
[9] Infrared Processing and Analysis Center, California Institute of Technology, MS 100-22, Pasadena, CA 91125, USA
[10] Istituto di Astrofisica e Planetologia Spaziali, INAF-IAPS, Via Fosso del Cavaliere 100, 00133 Roma, Italy

Received 26 October 2015 / Accepted 30 December 2015

ABSTRACT

A correlation between the 24 μm continuum and the [NII] 205 μm line emission may arise if both quantities trace the star formation activity on spatially-resolved scales within a galaxy, yet has so far only been observed in the nearby edge-on spiral galaxy NGC 891. We therefore assess whether the [NII] 205−24 μm emission correlation has some physical origin or is merely an artefact of line-of-sight projection effects in an edge-on disc. We search for the presence of a correlation in *Herschel* and *Spitzer* observations of two nearby face-on galaxies, M 51 and M 83, and the interacting Antennae galaxies NGC 4038 and 4039. We show that not only is this empirical relationship also observed in face-on galaxies, but also that the correlation appears to be governed by the star formation rate (SFR). Both the nuclear starburst in M 83 and the merger-induced star formation in NGC 4038/9 exhibit less [NII] emission per unit SFR surface density than the normal star-forming discs. These regions of intense star formation exhibit stronger ionization parameters, as traced by the 70/160 μm far-infrared (FIR) colour. These observations suggest the presence of higher ionization lines that may become more important for gas cooling, thereby reducing the observed [NII] 205 μm line emission in regions with higher star formation rates. Finally, we present a general relation between the [NII] 205 μm line flux density and SFR density for normal star-forming galaxies, yet note that future studies should extend this analysis by including observations with wider spatial coverage for a larger sample of galaxies.

Key words. galaxies: star formation – galaxies: spiral – galaxies: ISM – infrared: galaxies – ISM: lines and bands

1. Introduction

Diagnostic tracers of the star formation rate (SFR) have traditionally been based on observations of the broadband continuum (e.g. FUV, 24 μm band) or spectral line emission (e.g. Hα, Pα) of the Milky Way and nearby galaxies (see Kennicutt & Evans 2012 for a review, and references therein). The recent success of the *Herschel* Space Observatory (Pilbratt et al. 2010) is enabling the development of new SFR indicators at far-infrared (FIR) wavelengths (e.g. Li et al. 2013), particularly with the FIR fine-structure lines (e.g. De Looze et al. 2011, 2014; Farrah et al. 2013; Sargsyan et al. 2014; Pineda et al. 2014; Herrera-Camus et al. 2015). In the future, ground-based interferometers capable of observing these lines on spatially resolved (sub-arcsecond) scales, such as the Atacama Large Millimetre/sub-millimetre Array (ALMA) and the Northern Extended Millimetre Array (NOEMA), will allow us to trace the star formation activity out to the high-redshift Universe.

The [NII] 205 μm line is one such line, which originates from the $^3P_1 \rightarrow {}^3P_0$ transition of the ground state of singly ionized nitrogen. Nitrogen's ionization potential of 14.53 eV, which is slightly larger than that of hydrogen, means the [NII] emission traces all of the warm ionized interstellar medium (ISM). With a critical density for collisions with electrons of only 44 cm^{-3} at T = 8000 K (Oberst et al. 2006, 2011), the 205 μm line is highly susceptible to collisional excitation. The [NII] line also has the advantage that typically it is optically thin as a result of a small Einstein coefficient and, like other FIR lines, does not suffer from the problem of obscuration by interstellar dust that affects UV/optical tracers. Therefore, [NII] is expected to be an excellent indicator of SFR via measurement of the flux of ionizing photons.

For a sample of 70 galaxies in the *Herschel* Spectroscopic Survey of Warm Molecular Gas in Local Luminous Infrared Galaxies, Zhao et al. (2013) found that the SFR determined from the total infrared luminosity via the relationship in Kennicutt & Evans (2012) correlates with the integrated [NII] 205 μm line luminosity. More recently, Wu et al. (2015) found a spatially resolved correlation between the surface densities of the SFR and [NII] 205 μm line in the M 83 galaxy, and an intersection of the

local relationship and global relationship of Zhao et al. (2013) at high Σ_{SFR}. This finding suggests the latter correlation is dominated by active star-forming regions. Since the 24 μm and the [NII] 205 μm line emission both seem to trace the SFR on spatially resolved scales, one might expect to find a relationship between these two quantities.

In a recent study of the nearby edge-on spiral galaxy NGC 891, Hughes et al. (2015) exploited such an empirical relationship to predict the [NII] 205 μm line emission from a higher resolution 24 μm image. Although this appears to be a powerful and promising technique for estimating the [NII] 205 μm line emission from more widely available *Spitzer*-MIPS data, the underlying nature of the correlation is still unknown in part because of uncertainties associated with observations of high inclination systems. Integration along the line of sight through an edge-on spiral galaxy includes a range of physical environments, from active star-forming HII regions to diffuse ionized gas, making it difficult to interpret the origin of the relationship. In this paper, we thus attempt to assess whether the [NII] 205−24 μm correlation has some physical origin or is merely an artefact of line-of-sight projection effects in an edge-on disc. We search for the presence of a correlation in *Herschel* and *Spitzer* observations of face-on and interacting galaxies, and compare our findings to the NGC 891 correlation of Hughes et al. (2015). We show that not only is this empirical relationship also observed in face-on systems, but also that this correlation appears to be driven by the star formation rate. In the next section, we describe the data used for our analysis and in Sect. 3 we present our results. In Sects. 4 and 5, we discuss our results and conclusions, respectively.

2. Data and image processing

The Very Nearby Galaxy Survey (VNGS; P.I.: C. D. Wilson; see e.g. Parkin et al. 2013, 2014; Schirm et al. 2014; Hughes et al. 2014) is a *Herschel* Guaranteed Time Key Project that aims to study the gas and dust in the ISM of a diverse sample of 13 nearby galaxies with *Herschel*'s PACS and SPIRE instruments (see Pilbratt et al. 2010; Poglitsch et al. 2010; Griffin et al. 2010). This survey provides a unique dataset for investigating the spatially resolved [NII] 205 μm line emission. Observations with the SPIRE Fourier Transform Spectrometer (FTS) of the [NII] 205 μm line reach a ∼17″ spatial resolution. Because we require enough spatial coverage to accurately define and study the correlations, we select the late-type galaxies that have been observed in the high spectral resolution, intermediate (rather than sparse) spatial sampling mode. Our selection criteria include five objects: the edge-on spiral NGC 891, face-on spirals M 51 and M 83, and the interacting Antennae galaxies NGC 4038 and 4039 (4038/9 hereafter). Just as NGC 891 is the member of the sample that typifies an edge-on spiral, M 51 and M 83 are representative of face-on spiral galaxies and, thus, the most logical choices for a comparison with NGC 891. We also include the merging galaxies NGC 4038/9 to draw comparisons with more intense star-forming regions. Below, we summarize the available data and image processing steps.

2.1. SPIRE FTS [NII] line observations

The SPIRE FTS instrument (Griffin et al. 2010) consists of two bolometer arrays, the SPIRE Short Wavelength (SSW) array and the SPIRE Long Wavelength (SLW) array, covering wavelength ranges of 194 to 313 μm and 303 to 671 μm, respectively, with a 2′ diameter field of view. A complete description of the instrument may be found in the SPIRE Observers' Manual[1]. Intensity maps of the [NII] 205 μm line emission for NGC 891, M 51, M 83 and NGC 4038/9 have been presented in Hughes et al. (2015), Parkin et al. (2013), Wu et al. (2015) and Schirm et al. (2014), and we adopt the same distances of 9.6, 8.4, 3.6, and 20.0 Mpc, respectively. Here, we briefly summarize the observations and data reduction for each galaxy, whilst full details may be found in these corresponding papers.

In general, observations are reduced using HIPE with a SPIRE calibration context later than v.11.0.1 and basic standard processing steps. The observations for each galaxy consist of one central pointing in high spectral resolution intermediate-sampling mode, whilst for NGC 891 we also include publicly available open time observations (P.I.: G. Stacey) taken in sparse-sampling mode of the upper and lower portions of the disc. In all cases, we use the point-source calibrated data. Two spectral cubes corresponding to the SLW and SSW arrays are created via the *spireProjection* task, and the final spectra are fit with a polynomial and Sinc function for the baseline continuum and line emission. Wu et al. (2015) use the MPFIT procedure (Markwardt 2009) to fit the continuum and [NII] 205 μm line with parabolic and Sinc functions before the continuum-subtracted spectra are co-added in each area. Since all but M 83 were previously reduced using a homogeneous methodology, which is described in detail in Schirm et al. (2014), we chose to reprocess the M 83 observations in the same manner, using HIPE v.12.1 and SPIRE calibration context v.12.3. The final integrated [NII] flux maps have a 15″ pixel scale in the cases of NGC 891 and NGC 4038/9, whereas those of M 51 and M 83 have a 4″ pixel scale such that the finite pixels are centred on each of the bolometers of the FTS array, while the remaining pixels are left blank (cf. the [NII] maps in Fig. 1, left column). Our reprocessed M 83 intensity map is consistent within the errors to that of Wu et al. (2015).

2.2. MIPS 24 μm continuum observations

Our five chosen galaxies have 24 μm data obtained with the Multiband Imaging Photometer for *Spitzer* (MIPS; Rieke et al. 2004) and reprocessed by Bendo et al. (2012) using the MIPS Data Analysis Tools (Gordon et al. 2005) with some additional processing. Each image has a pixel scale of 1.″5, a PSF FWHM of 6″, and calibration uncertainties of ∼4% (Engelbracht et al. 2007). To facilitate a comparison between the [NII] intensity maps, our 24 μm maps were first convolved to the 17″ resolution of the [NII] 205 μm image with the common-resolution convolution kernels of Aniano et al. (2011), and rescaled to the appropriate pixel scale for each galaxy. Although these pixel sizes are typically smaller than the beam size, i.e. adjacent pixels are not independent, the analysis reproduces the same trends and conclusions as found when setting the pixel size equal to the beam size in each case. At the adopted distances, physical scales are 0.70, 0.61, 0.34 and 1.45 kpc for NGC 891, M 51, M 83 and NGC 4038/9, respectively.

3. Results

3.1. [NII] 205 μm line vs. 24 μm continuum correlation

Our first goal is to confirm the existence of a correlation in *Herschel* and *Spitzer* observations of M 51 and M 83, and

[1] Document HERSCHEL-DOC-0798 version 2.5 (March 2014), is available from the ESA *Herschel* Science Centre at http://herschel.esac.esa.int/Docs/SPIRE/spire_handbook.pdf

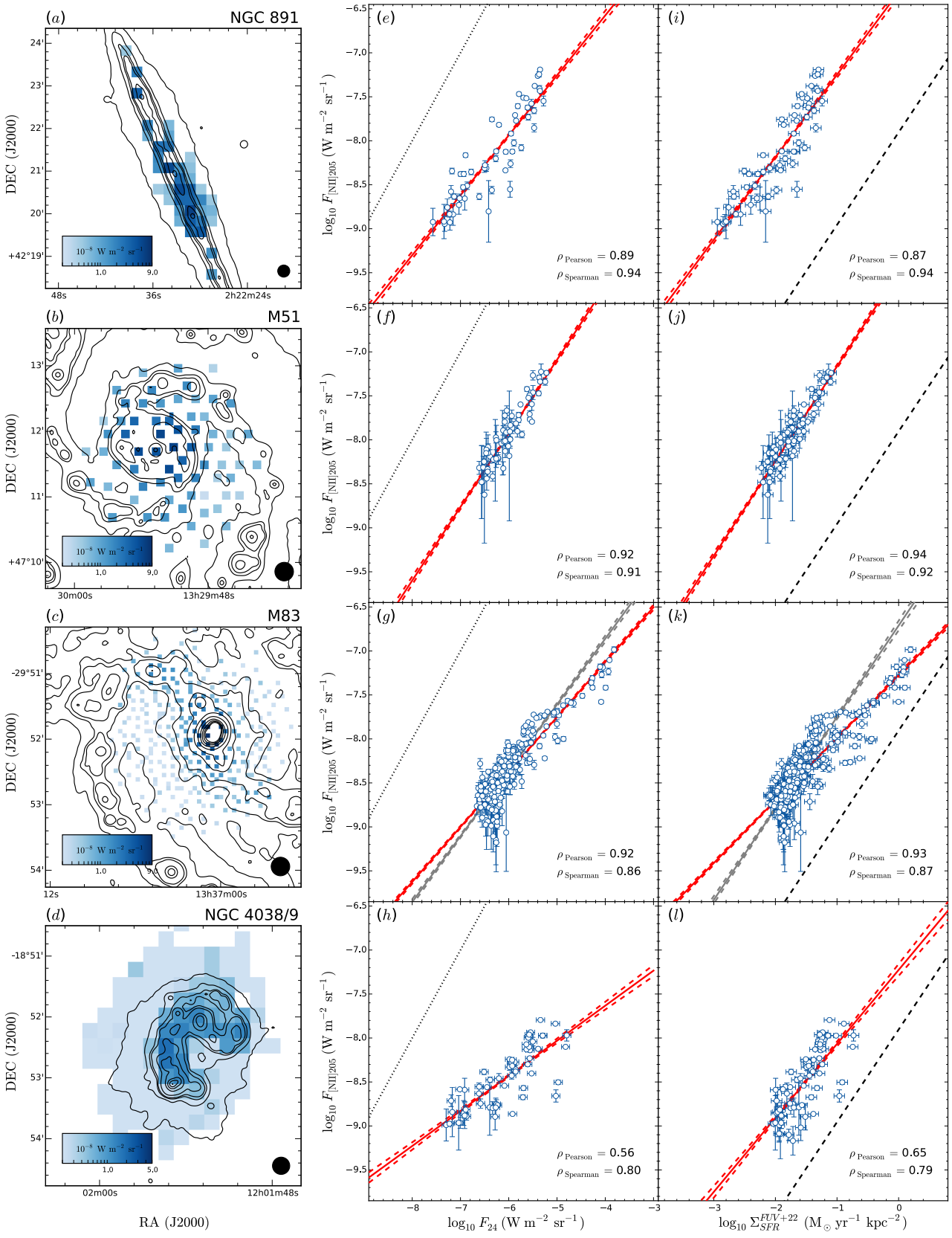

Fig. 1. For each galaxy (*rows*): SPIRE FTS [NII] 205 μm line emission maps at 17″ resolution (i.e. the beam size, indicated by a circle) superimposed on contours of constant 24 μm emission (*left panels*). The observed logarithms of the [NII] 205 μm line flux density versus 24 μm continuum flux density (*middle panels*) and $\Sigma_{\rm SFR}^{FUV+22}$ (*right panels*) are shown for each resolution element (blue circles). The scatter plots include the best linear fit (red solid line), 1σ confidence intervals (red dashed lines), the 1:1 relationship (dotted line), and the converted [NII] 205-SFR relation from integrated measurements (black dashed line) found by Zhao et al. (2013). The grey lines for M 83 indicate the best fit and confidence intervals obtained when excluding central pixels ($\log_{10} F_{24}$(W m^{-2} sr^{-1}) > −4.4). We state the Pearson and Spearman coefficients.

compare our findings to those of NGC 891. Such a correlation is already promisingly evident in the maps presented in the left column of Fig. 1: qualitatively, the brighter regions of the [NII] emission appear to correspond to the brighter contours of the 24 μm emission. In the middle column of Fig. 1, we quantify the correlation between [NII] 205 μm line emission and MIPS 24 μm emission for each galaxy. Figure 1e presents the original correlation in NGC 891 reported by Hughes et al. (2015). To briefly recap their results, the Spearman (ρ_S) and Pearson (ρ_P) coefficients of rank correlation are 0.94 and 0.88, respectively, where a value of 1 represents a perfect correlation. The best-fit linear relation is

$$\log_{10} F_{[NII]205} = (0.77 \pm 0.01) \log_{10} F_{24} - (3.31 \pm 0.04) \quad (1)$$

where both flux densities are in units of W m^{-2} sr^{-1}. In Fig. 1f and g, we present our results for the face-on galaxies, M 51 and M 83. The former galaxy shows a correlation of striking similarity to that of NGC 891. In fact, the Spearman and Pearson coefficients of 0.91 and 0.92 indicate a strong, linear correlation in log-log space. A best linear fit, expressed as Eq. (1) above, yields a gradient of 0.83 ± 0.02 and intercept equal to −2.90 ± 0.09, which is very similar to the best-fit relation to the NGC 891 observations. However, M 51's correlation has much less scatter and tighter 1σ confidence intervals, which are calculated from the residuals of the observations and the predictions given by the best-fit linear regression coefficients, compared to that of NGC 891.

The correlation is also evident in the case of M 83 with similar Spearman (0.86) and Pearson (0.92) coefficients. The best-fit linear relation deviates away from the 1:1 relationship for the regions of brighter 24 μm flux density, unlike M 51 and NGC 891, and has a gradient and intercept of 0.50 ± 0.01 and –5.42 ± 0.03, respectively. The difference in the correlation appears to be driven by the central pixels which are very bright in the 24 μm band yet have lower [NII] line emission than we would expect from the other two cases. Bendo et al. (2012) warn that the central 8″ of the galaxy is saturated in the 24 μm map. In the event that this saturation causes an issue in our convolution and rescaling of the 24 μm map to match the properties of the [NII] intensity map, we also examine the best-fit linear relation when removing these central pixels (grey lines in Fig. 1g), finding little variation in slope or intercept of the linear best fit. Finally, NGC 4038/9 displays an albeit weaker correlation (Fig. 1h). In Table 1, we summarize the coefficients of the best linear fits.

Table 1. Best-fit relations between the [NII] 205 μm line emission and various parameters considered in this work, expressed as $\log_{10}(F_{[NII]205}/\mathrm{W\ m^{-2}\ sr^{-1}}) = c + m \log_{10} x$, with the corresponding 1σ errors.

Galaxy	m	c	σ	ρ_P	ρ_S
$x \equiv F_{24}$/W m^{-2} sr^{-1}					
NGC 891	0.77 ± 0.01	–3.31 ± 0.04	0.36	0.89	0.94
M 51	0.83 ± 0.02	–2.90 ± 0.09	0.16	0.92	0.91
M 83 (all)	0.50 ± 0.01	–5.42 ± 0.03	0.37	0.92	0.86
M 83 (limited)	0.58 ± 0.02	–4.93 ± 0.08	0.20	0.94	0.86
NGC 4038/9	0.40 ± 0.02	–6.04 ± 0.05	0.40	0.56	0.80
$x \equiv \Sigma_{SFR}^{FUV+22}/M_\odot$ yr^{-1} kpc^{-2}					
NGC 891	0.94 ± 0.02	–6.31 ± 0.04	0.22	0.87	0.94
M 51	1.07 ± 0.02	–6.09 ± 0.04	0.14	0.94	0.92
M 83 (all)	0.71 ± 0.01	–7.27 ± 0.01	0.28	0.87	0.93
M 83 (limited)	1.04 ± 0.02	–6.71 ± 0.04	0.19	0.78	0.74
NGC 4038/9	0.84 ± 0.03	–7.22 ± 0.05	0.22	0.65	0.79
$x \equiv \Sigma_{SFR}^{FUV+24}/M_\odot$ yr^{-1} kpc^{-2}					
NGC 891	0.72 ± 0.01	–6.59 ± 0.02	0.35	0.87	0.91
M 51	0.90 ± 0.02	–6.29 ± 0.03	0.14	0.92	0.90
M 83 (all)	0.66 ± 0.01	–7.19 ± 0.01	0.33	0.87	0.92
M 83 (limited)	0.86 ± 0.01	–6.79 ± 0.02	0.16	0.81	0.87
NGC 4038/9	0.52 ± 0.02	–7.52 ± 0.03	0.39	0.88	0.84

Notes. We also state the scatter in dex (σ), Spearman (ρ_S), and Pearson (ρ_P) coefficients. For M 83, the limited case excludes the central pixels ($\log_{10} F_{24}$(W m^{-2} sr^{-1}) > −4.4).

3.2. [NII] 205 μm line as a SFR tracer

We suspect the correlation between the [NII] 205 μm line emission and the 24 μm continuum may be originating from the capability of both quantities to trace the star formation activity on spatially resolved scales. Even if the [NII] line emission and SFR both correlate with the 24 μm emission, this does not automatically imply that the [NII] line should also correlate with the SFR. For example, the SFR could also be dependent on the diffuse UV emission not associated with the warm ISM around young stars. An immediate test of this hypothesis is to investigate the relationship of the [NII] 205 μm line emission from each region to the local SFR surface density, Σ_{SFR}. Although the 24 μm band is often used as a star formation tracer (see e.g. Calzetti et al. 2005, 2007), it is important to test any relation between [NII] and Σ_{SFR} independent of the 24 μm continuum. We therefore estimate Σ_{SFR} with a multi-wavelength composite tracer (see e.g. Kennicutt & Evans 2012), adopting the SFR calibration of Hao et al. (2011) for a linear combination of the FUV flux from Galaxy Evolution Explorer (GALEX, Martin et al. 2005) observations and mid-IR flux from Wide-field Infrared Survey Explorer (WISE, Wright et al. 2010) 22 μm maps (both convolved and rescaled to match the resolution and pixel size of the [NII] map), in order to correct the UV for dust attenuation independent of the MIPS 24 μm data. However, we also examined the trends using the SFR based on the 24 μm data, Σ_{SFR}^{FUV+24}, and note, as previously observed by Lee et al. (2013), very little difference between the two tracers.

In the right panels of Fig. 1, we compare the [NII] 205 μm line emission to the SFR surface density, Σ_{SFR}^{FUV+22}. Remarkably, the [NII] emission correlates with the SFR in a similar fashion as the observed 24 μm flux density in all five galaxies (cf. the middle and right columns). Again, we find that the relations for the discs of NGC 891 and M 51 are similar, yet M 83 and NGC 4038/9 have shallower slopes (see Table 1). Interestingly, the former two objects form a relation lying almost parallel to that seen for the integrated galaxy quantities in Zhao et al. (2013), whereas NGC 4038/9 and the central regions of M 83 have much higher SFRs than their [NII] line emission would suggest (see also Fig. 8 of Wu et al. 2015).

Perhaps the fact that the [NII]– Σ_{SFR} correlation differs in the cases of M 83 and NGC 4038/9 compared to the other two normal star-forming galaxies is not so surprising, for the following reasons. Firstly, the centre of M 83 is atypical in that it exhibits a double nucleus in addition to a nuclear starburst (see Wu et al. 2015, and references therein). The higher SFRs driven by the starburst partly govern the slope of best-fit [NII] 205 – Σ_{SFR} relation; omitting the central nine pixels covering the nucleus and bar from the linear regression uncovers a best-fit line with a slope similar to that found for the other two galaxies (see the grey lines

in Fig. 1k). Similar to the nucleus of M 83, the Antennae galaxies also exhibit high SFRs, likely from merger-triggered star formation: estimates suggest a stellar mass of $\sim 2.5 \times 10^8$ $M_\odot$ has been formed in $\sim 7 \times 10^6$ years (Fischer et al. 1996). Secondly, the SPIRE FTS observations of NGC 891 and M 51 cover a greater fraction of the star-forming regions as traced by the 24 μm emission than those of M 83, where nearly 40% of the pixels cover the inter-arm regions with lower levels of star formation (see Fig. 1, left column). We can only speculate that a hypothetical increase of the spatial coverage of the M 83 observations to include more of the spiral arms/star-forming disc (and still omitting the nucleus) would yield a [NII] 205−SFR relationship with slope and scatter similar to the other two galaxies.

4. Discussion

We have shown that the [NII] 205−24 μm emission correlation is present in nearby face-on star-forming discs, indicating the relationship is unlikely to be an artefact arising from line-of-sight projection effects and lending credence to the notion of a physical origin. In addition, a preliminary analysis of VNGS target NGC 2403 yields similar results (Hughes et al., in prep.). At present, the strong correlation between the [NII] emission and the star formation rate surface density, which is traced with two independent measures of the mid-IR continuum, suggests that the recent star formation history is driving this empirical relation.

The limitations of this analysis are clear. Firstly, as mentioned in Hughes et al. (2015), despite the high quality of observations of the far-infrared, fine-structure lines made possible by the *Herschel* Space Observatory, which enable us to resolve features on sub-kiloparsec scales, one of the main restrictions was the relatively sparse coverage and low spatial resolution of the [NII] 205 μm line. There is also uncertainty in the SFR calibration. The FUV emission predominately traces massive ($M > 10-15$ $M_\odot$) stars that typically survive for <30 Myr, whereas the 22 and 24 μm emission traces mostly dust in HII star-forming regions, which probes lower mass (~ 4 $M_\odot$) stars with lifetimes of a few hundred Myr on the main sequence. Thus, these two quantities both probe different timescales of recent star formation (see Kennicutt & Evans 2012). Different star formation histories for different regions leads to changes in the relative importance of the FUV and the 22 or 24 μm emission, and therefore may produce regional variations in the calibration (e.g. Boquien et al. 2014). Further complications arise when considering that asymmetric migration of photoionizing stars <4 Myr in age from their birth sites in spiral density waves may introduce a spatial offset in UV emission and 24 μm emission (see Fig. 8 in Jones et al. 2015), and that stochastically heated dust associated with HI gas also emits in the 22 μm band (see e.g. Eufrasio et al. 2014).

Momentarily casting these issues aside, the fact remains that, if we adopt the correlations found in the cases of NGC 891 and M 51, then the higher star formation rates in NGC 4038/9 and the centre of M 83 associated with a nuclear starburst would be under-predicted by the observed [NII] 205 μm line flux. Practically, the [NII] 205 μm line is not an ideal SF tracer. This raises the question of by what mechanism(s), or under which physical conditions, does the [NII] 205 μm line cease to be a tracer of star formation and/or the underlying nature of the correlation change. One possible explanation arises when we consider that heating in ionized gas is mainly due to photoionization, and, therefore, depends strongly on the critical electron density and the ionization parameter, U. This parameter is defined as the dimensionless ratio of the number density of incident ionizing photons to the number density of hydrogen nuclei. Theoretical models predict that IR colours can act as approximate tracers of U, whereby $\log U$ increases with the IR colour (see e.g. the $\nu F_\nu(60\,\mu\text{m})/\nu F_\nu(100\,\mu\text{m})$ colours in Abel et al. 2009).

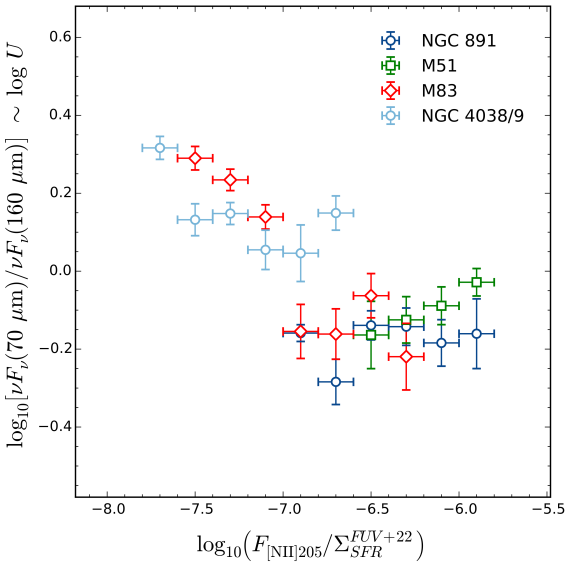

Fig. 2. Far-infrared colour $\nu F_\nu(70\,\mu\text{m})/\nu F_\nu(160\,\mu\text{m})$ versus the ratio of the [NII] emission in W m^{-2} sr^{-1} to the SFR in $M_\odot$ yr^{-1} kpc^{-2} for each galaxy, where points represent the median in bins along the abscissa of width indicated by the error bars.

In Fig. 2, we plot the $\nu F_\nu(70\,\mu\text{m})/\nu F_\nu(160\,\mu\text{m})$ FIR colour[2] versus the ratio of the [NII] emission (in W m^{-2} sr^{-1}) to the SFR (in $M_\odot$ yr^{-1} kpc^{-2}) for each galaxy. The range and mean of the FIR colour is evidently similar for the normal star-forming discs, except for a clear offset in the FIR colour of M 83 and NGC 4038/9, which coincides with low [NII] emission per SFR values. Similar trends emerge when alternatively using the 70/250 and 160/250 μm FIR colours. Our observations suggest that the ionization parameter is much higher in these regions compared to the rest of the M 83 galaxy and the other two discs. Therefore, we expect higher ionization lines (e.g. [NIII] 57 μm) to play a greater role in the cooling of the gas, which could also partly explain the lower $F_{[\text{NII}]205}/\Sigma_{\text{SFR}}$ ratios. It is also possible that dust obscuration becomes more effective in more compact star-forming regions (e.g. at increasing FIR colour), such that more ionizing photons go towards dust heating instead of gas heating leading to a decreasing [NII]/Σ_{SFR} ratio (see Díaz-Santos et al. 2013). Furthermore, the Zhao et al. (2013) [NII] 205 – SFR relation was defined based on observations of LIRGS, which are known to have strong ionization parameters (e.g. Petric et al. 2011), so it may not be so surprising that the M 83 nucleus with its high U falls on this relation (as found in Wu et al. 2015) in contrast to the behaviour observed in regions with low values of the ionization parameter.

From these results, we attempt to derive a general relation between the [NII] 205 μm line flux density and star formation rate for main-sequence star-forming galaxies. We first discard regions with very high (>0.2, see Fig. 2) 70/160 μm FIR colours, which in practice is equivalent to omitting pixels where $\log_{10} F_{24}$(W m^{-2} sr^{-1}) > −5.1 (cf. Fig. 1g and 1h), and examine the Σ_{SFR}–$F_{[\text{NII}]205}$ correlations for all galaxies (see Fig. 3).

[2] Homogeneous VNGS *Herschel* PACS and SPIRE photometric maps are available on HeDaM at http://hedam.lam.fr/VNGS/data.php

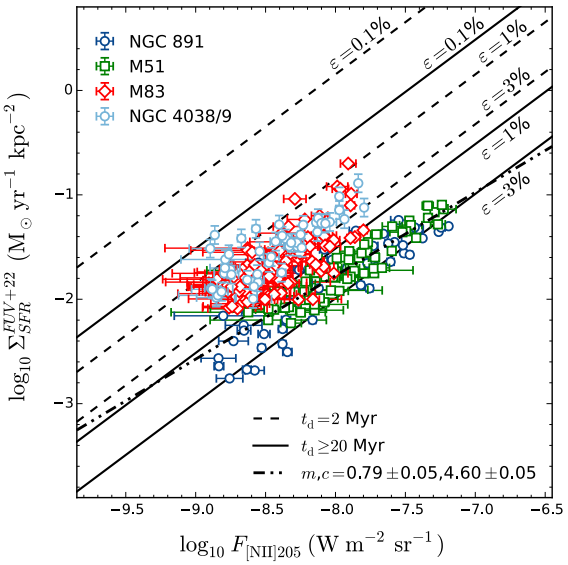

Fig. 3. The $\Sigma_{SFR} - F_{[NII]205}$ correlation superimposed on the predictions from the *Starburst*99 model. For varying values of ε, the dashed lines correspond to a stellar population with a constant SFR and t_d = 2 Myr, and solid lines correspond to $t_d \geq 20$ Myr. The dash-dotted line is the best-fitting linear relation from the M 51 and NGC 891 data.

Simply combining all the data to define an average relation is prevented by the aforementioned offset in the individual galaxy relations. To interpret this offset, we use the *Starburst*99 stellar population synthesis code (Leitherer et al. 1999) to model the Σ_{SFR}–$F_{[NII]205}$ relation following the approach of Herrera-Camus et al. (2015), who consider that gas heating by FUV photons emitted from star-forming regions relate to gas cooling from the [NII] line via the photoelectric effect in PAHs and dust grains. In brief, we assume a stellar population with a constant SFR over 100 Myr and solar metallicity[3] and adopt the Geneva evolutionary tracks (zero rotation) and Kroupa initial mass function. From the resulting spectrum, given as a function of the duration of the star formation episode, t_d, we integrate across the energy range of photons that dominate the dust grain photoelectric heating, specifically $6 < E_\gamma < 13.6$ eV. The product of the fraction of these FUV photons responsible for the photoelectric heating of dust grains and the photoelectric heating efficiency of the dust gives the overall heating efficiency, ε, which we vary between 0.1 and 3% to estimate the amount of gas heating. We further assume that the cooling of the gas is typically dominated by the [CII] transition and that the [CII]/[NII]205 line ratio theoretically varies around ~4 for a range of electron densities (see Oberst et al. 2006). The [NII] and FUV flux densities are then related by $F_{[NII]} \sim 0.25\, \varepsilon\, F_{FUV}(t_d)$ for a given Σ_{SFR}.

Comparing the model predictions to the observations in Fig. 3, we find the vast majority of regions in NGC 891 and M 51 may have been actively forming stars for $t_d \geq 20$ Myr with ε between 1 and 3%. As a result of the model degeneracy between t_d and ε (see Herrera-Camus et al. 2015 for details), M 83 and NGC 4038/9 exhibit a stellar population with either a star formation duration of $t_d \geq 20$ Myr and $\varepsilon \lesssim 1\%$ or more recent star formation episodes of t_d = 2 Myr and ε between 1 and 3%. This suggests that these two galaxies also possess regions with higher SFRs from recently triggered star formation, likely due to the merger (NGC 4038/9) or central starburst (M 83), as we discuss above. We thus combine the NGC 891 and M 51 data, representing normal star-forming regions, to define the best-fit relation as

$$\log_{10} \Sigma_{SFR} = (0.79 \pm 0.05) \log_{10} F_{[NII]205} + (4.60 \pm 0.05), \quad (2)$$

which is valid in the ranges of $-8.9 < \log_{10} F_{[NII]205} < -7.5$ and $-2.4 < \log_{10} \Sigma_{SFR} < -1.2$, where the units are as stated previously. The scatter, defined as the standard deviation of the residuals between the observed and predicted Σ_{SFR}, is ±0.10 dex. A similar yet offset relation to Eq. (2) is formed by M 83 and NGC 4038/9 with a gradient m of 0.69 ± 0.05, y intercept of 4.38 ± 0.05 and a 0.16 dex scatter. We stress, however, all of the caveats and issues we mention above, especially the small sample size, that should be considered when using these relations for estimating the star formation rate.

5. Conclusions

In this paper, we aimed to test whether the [NII] 205 – 24 μm emission correlation observed in NGC 891 arises from line-of-sight projection effects in an edge-on disc. Using *Herschel* and *Spitzer* observations of two nearby face-on galaxies, M 51 and M 83, and the interacting Antennae galaxies NGC 4038 and 4039, we have shown that not only is this empirical relationship also observed in face-on galaxies, but also that the correlation appears to be governed by the star formation rate (SFR). Both the nuclear starburst in M 83 and the merger-induced star formation in NGC 4038/9 exhibit less [NII] emission per unit SFR surface density than the normal star-forming discs. These regions of intense star formation exhibit stronger ionization parameters, as traced by the 70/160 μm far-infrared colour. The stronger ionization parameters suggest the presence of higher ionization lines that may become more important for gas cooling, thereby reducing the observed [NII] 205 μm line emission in regions with higher star formation rates. Alternatively, dust obscuration may become more effective in more compact star-forming regions, meaning more ionizing photons go towards dust heating instead of gas heating. We used a simple model based on *Starburst*99 to predict the Σ_{SFR}–$F_{[NII]205}$ relation; we found that regions with more recent star formation in the merging Antennae galaxies NGC 4038/9 and the central starburst in M 83 likely cause the offsets in [NII] emission per unit SFR surface density found between these galaxies and the normal star-forming discs. Finally, we present a general relation between the [NII] 205 μm line flux density and star formation rate for main-sequence star-forming galaxies.

Clearly, future studies should seek to analyse spatially resolved observations of other FIR lines (e.g. [NII] 122, [CI] 370 μm) for a larger sample that includes not only central regions of galaxies, but also sites of star formation along the spiral arms. Although observations of [NII] 205 μm can be followed up over a large redshift range by facilities such as NOEMA and ALMA, which can observe the line emission at $z \sim 0.6$ in band-10 and at $z \sim 3.2$ in band-7, care should be taken in the use of the line as a star formation tracer given the apparent dependency of the local [NII] emission on the ionization parameter.

Acknowledgements. We thank the anonymous referee for the useful comments and suggestions that helped to improve this paper. T.M.H. and E.I. acknowledge CONICYT/ALMA funding Program in Astronomy/PCI Project N°:31140020. T.M.H. also acknowledges the financial support from the Belgian Science Policy Office (BELSPO) in the frame of the PRODEX project C90370 (Herschel-PACS Guaranteed Time and Open Time Programs: Science Exploitation). M.B. and I.D.L. acknowledge the financial support of the Flemish Fund for Scientific Research (FWO-Vlaanderen). SPIRE was developed by a consortium

[3] For $Z = 0.2\, Z_\odot$, the y-intercepts of the model lines in Fig. 3 increase by a factor of 0.01 (i.e. lines shift upwards).

of institutes led by Cardiff University (UK) and including Univ. Lethbridge (Canada); NAOC (China); CEA, LAM (France); IFSI, Univ. Padua (Italy); IAC (Spain); Stockholm Observatory (Sweden); Imperial College London, RAL, UCL-MSSL, UKATC, Univ. Sussex (UK); and Caltech, JPL, NHSC, Univ. Colorado (USA). This development has been supported by national funding agencies: CSA (Canada); NAOC (China); CEA, CNES, CNRS (France); ASI (Italy); MCINN (Spain); SNSB (Sweden); STFC, UKSA (UK); and NASA (USA). This research made use of APLpy, an open-source plotting package for Python hosted at http://aplpy.github.com.

References

Abel, N. P., Dudley, C., Fischer, J., Satyapal, S., & van Hoof, P. A. M. 2009, ApJ, 701, 1147
Aniano, G., Draine, B. T., Gordon, K. D., & Sandstrom, K. 2011, PASP, 123, 1218
Bendo, G. J., Galliano, F., Madden, S. C., et al. 2012, MNRAS, 423, 197
Boquien, M., Buat, V., & Perret, V. 2014, A&A, 571, A72
Calzetti, D., Kennicutt, Jr., R. C., Bianchi, L., et al. 2005, ApJ, 633, 871
Calzetti, D., Kennicutt, R. C., Engelbracht, C. W., et al. 2007, ApJ, 666, 870
De Looze, I., Baes, M., Bendo, G. J., Cortese, L., & Fritz, J. 2011, MNRAS, 416, 2712
De Looze, I., Cormier, D., Lebouteiller, V., et al. 2014, A&A, 568, A62
Díaz-Santos, T., Armus, L., Charmandaris, V., et al. 2013, ApJ, 774, 68
Engelbracht, C. W., Blaylock, M., Su, K. Y. L., et al. 2007, PASP, 119, 994
Eufrasio, R. T., Dwek, E., Arendt, R. G., et al. 2014, ApJ, 795, 89
Farrah, D., Lebouteiller, V., Spoon, H. W. W., et al. 2013, ApJ, 776, 38
Fischer, J., Shier, L. M., Luhman, M. L., et al. 1996, A&A, 315, L97
Gordon, K. D., Rieke, G. H., Engelbracht, C. W., et al. 2005, PASP, 117, 503
Griffin, M. J., Abergel, A., Abreu, A., et al. 2010, A&A, 518, L3
Hao, C.-N., Kennicutt, R. C., Johnson, B. D., et al. 2011, ApJ, 741, 124
Herrera-Camus, R., Bolatto, A. D., Wolfire, M. G., et al. 2015, ApJ, 800, 1
Hughes, T. M., Baes, M., Fritz, J., et al. 2014, A&A, 565, A4
Hughes, T. M., Foyle, K., Schirm, M. R. P., et al. 2015, A&A, 575, A17
Jones, A. G., Bendo, G. J., Baes, M., et al. 2015, MNRAS, 448, 168
Kennicutt, R. C., & Evans, N. J. 2012, ARA&A, 50, 531
Lee, J. C., Hwang, H. S., & Ko, J. 2013, ApJ, 774, 62
Leitherer, C., Schaerer, D., Goldader, J. D., et al. 1999, ApJS, 123, 3
Li, Y., Crocker, A. F., Calzetti, D., et al. 2013, ApJ, 768, 180
Markwardt, C. B. 2009, in Astronomical Data Analysis Software and Systems XVIII, eds. D. A. Bohlender, D. Durand, & P. Dowler, ASP Conf. Ser., 411, 251
Martin, D. C., Fanson, J., Schiminovich, D., et al. 2005, ApJ, 619, L1
Oberst, T. E., Parshley, S. C., Stacey, G. J., et al. 2006, ApJ, 652, L125
Oberst, T. E., Parshley, S. C., Nikola, T., et al. 2011, ApJ, 739, 100
Parkin, T. J., Wilson, C. D., Schirm, M. R. P., et al. 2013, ApJ, 776, 65
Parkin, T. J., Wilson, C. D., Schirm, M. R. P., et al. 2014, ApJ, 787, 16
Petric, A. O., Armus, L., Howell, J., et al. 2011, ApJ, 730, 28
Pilbratt, G. L., Riedinger, J. R., Passvogel, T., et al. 2010, A&A, 518, L1
Pineda, J. L., Langer, W. D., & Goldsmith, P. F. 2014, A&A, 570, A121
Poglitsch, A., Waelkens, C., Geis, N., et al. 2010, A&A, 518, L2
Rieke, G. H., Young, E. T., Engelbracht, C. W., et al. 2004, ApJS, 154, 25
Sargsyan, L., Samsonyan, A., Lebouteiller, V., et al. 2014, ApJ, 790, 15
Schirm, M. R. P., Wilson, C. D., Parkin, T. J., et al. 2014, ApJ, 781, 101
Wright, E. L., Eisenhardt, P. R. M., Mainzer, A. K., et al. 2010, AJ, 140, 1868
Wu, R., Madden, S. C., Galliano, F., et al. 2015, A&A, 575, A88
Zhao, Y., Lu, N., Xu, C. K., et al. 2013, ApJ, 765, L13